JOURNAL OF AIRCRAFT
Vol. 44, No. 1, January–February 2007

Experimental Investigation of Vectoring Jet on Aerodynamic Characteristics of Aircraft

Wang Yankui,* Deng Xueying,† and Zhang Yongsheng‡
Beijing University of Aeronautics and Astronautics, 100083 Beijing, China

DOI: 10.2514/1.22964

Thrust vectoring is one of the advanced technologies in the design of the fourth generation fighter to provide high maneuverability and agility. The purpose of this paper is to investigate the effect of the vectoring jet on aerodynamic characteristics of a modern fighter. The tests are conducted in a transonic wind tunnel with a square test section of 0.6 × 0.6 m and a low speed wind tunnel with a 0.8 × 1 m elliptical test section. The test results are obtained at a Mach number of 0.4 or 0.8 and a Reynolds number of 9.5×10^6 or 15.6×10^6 per meter at angles of attack ranging from 0 to 23 deg for a high speed test, and at 45 m/s for a low speed test and Reynolds number of 3×10^6 per meter at angles of attack ranging from 0 to 45 deg. High-pressure air is used to simulate the jet flow, and the nozzle pressure ratio is varied from 1.0 (jet off) to 4. One modern fighter model is employed and divided into two parts of forebody and afterbody for force-measuring, respectively. As a result, the interaction behaviors are obtained.

Nomenclature

b	=	wing mean geometric chord
C_D	=	drag coefficient $[D/(qS_{\text{ref}})]$
C_{D0}	=	zero-lift drag coefficient
C_L	=	lift coefficient $[L/(qS_{\text{ref}})]$
$C_{L\alpha}$	=	derivation of lift coefficient with respect to the angle of attack $(\partial C_L/\partial\alpha)$
C_m	=	pitching moment coefficient $[M/(qS_{\text{ref}}b)]$
C_p	=	pressure coefficient $[C_p = (p_i - p_\infty)/q]$
H	=	the aerodynamic forces or moments acting on the model on conditions of $M_\infty \neq 0$ and jet on except for direct thrust component
M	=	pitching moment
M_∞	=	freestream Mach number
p_i	=	the static pressure on the model surface
p_{tj}	=	jet total pressure
p_∞	=	freestream static pressure
q	=	dynamic pressure
S_{ref}	=	reference area
s	=	wing span
V_∞	=	speed of free stream
α	=	the angle of attack (deg)
α_s	=	stalled angle of attack (deg)
α'	=	effective angle of attack (deg)
δ_j	=	deflection angle of vectoring jet (deg)
δ_ϕ	=	deflection angle of horizontal tail (deg)
δ_{CL}	=	the jet-induced or supercirculation effect of vectoring jet on the lift C_L
δ_{Cm}	=	the jet-induced or supercirculation effect of vectoring jet on the pitching moment C_m
δ_{CD}	=	the jet-induced or supercirculation effect of vectoring jet on the drag C_D
ρ	=	the density of atmosphere

Received 3 February 2006; revision received 7 March 2006; accepted for publication 28 April 2006.

*Professor, Institute of Fluid Mechanics, 37#, xueyuanlu, Haidian District.
†Professor, Institute of Fluid Mechanics, 37#, xueyuanlu, Haidian District. Senior Member AIAA.
‡Graduate Student, Institute of Fluid Mechanics, 37#, xueyuanlu, Haidian District.

I. Introduction

WITH the demand of high maneuverability and agility for the modern fighter, extensive investigation has been conducted on employing the aircraft propulsion system as a potential source for additional maneuvering power [1–4]. To achieve the multimission capability, thrust vectoring/reversing is one of the key technologies and is widely applied to the design of the modern fighter. Thrust vectoring can provide large control moments that are independent of angle of attack by producing a component of thrust perpendicular to the body longitudinal axis. At high angles of attack, the pitching and yawing moments required for controlling aircraft can be produced by the direct thrust component when the aerodynamic control surfaces of the aircraft work inefficiently [5,6]. In addition, a strong jet-induced or supercirculation effect on the aerodynamics of aircraft must be investigated for flight control [7–15]. Based on the fighter configuration shown in Fig. 1, a detailed investigation of the effects of vectoring jet-on aerodynamic characteristics is given in this paper.

II. Apparatus and Procedure

A. Wind Tunnel and Air Tank

The tests are conducted in the FL-1 wind tunnel in Shenyang Aerodynamic Research Institute and $D1$ wind tunnel in Beijing University of Aeronautics and Astronautics. The FL-1 wind tunnel is a transonic one with a square test section of 0.6×0.6 m. The test Mach number in this wind tunnel is 0.4 or 0.8, and the corresponding Reynolds number is 9.5×10^6 or 15.6×10^6 per meter. The $D1$ is a low speed wind tunnel with an 0.8×1 m^2 elliptical test section and the velocity of free stream is 45 m/s. To provide thrust vectoring effect, a series of nozzles with different deflected angles are made and the deflection angles range from −20 to 20 deg.

The jet is provided by the air tank with the maximum pressure 2.0 MPa at constant temperature and is ducted to the model through the model support and the forebody balance, as shown in Fig. 2. This high-pressure air is then transferred into the after-fuselage of the model by means of two flow-transfer assemblies (see the sketch of Fig. 2). Flexible metal bellows are located in each end of the flow-transfer assemblies and act to compensate for axial forces caused by pressurization as well as provide a leak-free assembly. Extensive jet-on calibrations with nozzles are performed, before the investigation, under known load conditions to determine bellows and flow-transfer tare forces. In addition, the jet exhaust conditions are measured in the instrumentation section upstream of the nozzles. The instrumentation consists of 4 total-pressure and 4 static probes. The total volume of the air tank is 200 m^3. From the results of pretest, this capacity of air support system can provide the desired NPR [nozzle pressure ratio (p_{tj}/p_∞)] requirement. At the same time, the system can also

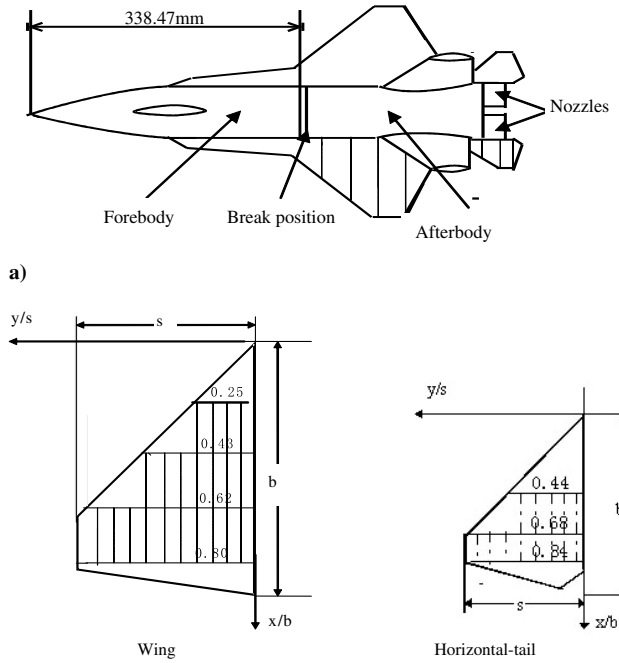

Fig. 1 a) Model configuration and b) distribution of pressure-measuring section and position.

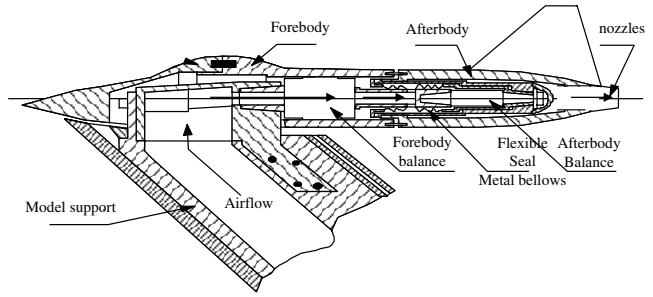

Fig. 2 The sketch of jet assembly and balances.

keep the pressure setting within 0.5% of precision during the period of each testing.

B. Model and Balance

As shown in Figs. 1 and 2, the 1/32 scale model used in this investigation is a modern fighter configuration and features a wing with 42 deg swept leading edge and strake, horizontal tail with 42 deg swept leading edge and afuselage with twin-vertical tail. The twin axisymmetric exhaust nozzles, which are installed at the end of the model, are changeable for different a deflecting angle from $\delta_j = -20$ to 20 deg so as to achieve the thrust vectoring. The model is divided into two parts so that the vectoring jet effect on aerodynamic performance of forebody and afterbody can be studied separately by installing them on two six-component balances, respectively. The term afterbody, as used in this paper, refers to the portion after break position (in Figs. 1 and 2) on which forces and moments are measured by a six-component force balance, namely the afterbody balance as shown in Fig. 2. The break position is located at position 338.47 mm from the model top and the afterbody consists of the after-fuselage and empennages including the horizontal tail with a 42 deg swept leading edge and a vertical tail. The forebody refers to the portion before break position and includes the fore fuselage and wing, as shown in Figs. 1 and 2, on which the forces and moments are measured by the six-component forebody balance, illustrated in Fig. 2. These two six-component internal balances are used in these tests to measure the forces and moments acting on the forebody and afterbody of the model, respectively. Moreover, the direct thrust components produced by the vectoring jet can also be measured independently by the ϕ20 mm afterbody balance on condition of $M_\infty = 0$ and jet on. Figure 2 shows the general information of the component arrangement and the jet assembly of the test system.

C. Data Processing

At the beginning of the test, the balances are calibrated to determine the sensitivity and interaction characteristics of each component. For the two six-component strain-gage balances used in this test, the calibration results in the following precision: normal force, 0.1%; side force, 0.2%; axial force, 0.5%; rolling moment, 0.5%; pitching moment, 0.3%; yawing moment, 0.5%. Additionally, the pressure transducers are also calibrated by a standard air pressurized system and the accuracy is within ± 5 Pa. The accuracy of α is also calibrated to be within ± 0.05 deg and the accuracy of Mach number of the freestream is within ± 0.03.

The test range of the angle of attack is from 0 to 22 deg for high speed conditions and 0 to 45 deg for low speed conditions. For each data point, 1000 frames of data are taken over a period of time and the average value is used for computation. The force and moment coefficient of the forebody and afterbody balance are non-dimensionalized by freestream dynamic pressure, wing reference area (0.068359 m^2), wing mean geometric chord (0.1935 m), and wing span (0.41337 m). Most of the data presented are plotted as a function of the model angle of attack or spanwise of the wing and horizontal tail.

The jet-induced or supercirculation effect on the aerodynamics of the model, which is labeled as δ_* (where * can be replaced by C_L, C_m, C_D, or other aerodynamic coefficients, such as δ_{CL}, δ_{Cm}, δ_{CD}, etc.), can be obtained from the following equation:

$$\delta_* = \mathrm{WJ–WO–JO} \tag{1}$$

where, the symbols "WJ" , "WO", and "JO" stand for the aerodynamic forces or moments acting on the model on conditions of $M_\infty \neq 0$ and jet on including direct thrust component, $M_\infty \neq 0$ and jet off, $M_\infty = 0$ and jet on for direct thrust component measuring, respectively. Additionally,

$$H = \mathrm{WJ–JO} \tag{2}$$

where, the symbol "H" stands for aerodynamic forces or moments acting on the model on conditions of $M_\infty \neq 0$ and jet on except for the direct thrust component.

III. Results and Discussions

A. Aerodynamic Characteristics of Model Without Vectoring Jet

1. *Aerodynamic Characteristics of Forebody Without Jet*

Figure 1 shows the variation of lift coefficient C_L of the forebody with respect to angles of attack without vectoring jet, in which δ_ϕ is the deflection angle of horizontal tail, δ_j is the deflection angle of nozzles. It can be found from the Fig. 3:

1) The stalled angle of attack (α_s) of the forebody decreases as freestream Mach number M_∞ increases at the same δ_ϕ and δ_j. When $\alpha > \alpha_s$, the slope of lift curve $C_{L\alpha}$ decreases quickly, even $C_{L\alpha} < 0$ due to the bursted leading edge vortices above the wing. The flows over the forebody at $\alpha > 14$ deg for $M_\infty = 0.8$ and $\alpha > 18$ deg for $M_\infty = 0.4$ belong to this type.

2) As shown in Fig. 3, the lift coefficient C_L increases with the δ_ϕ increasing obviously (when the trailing edge of the horizontal tail is deflected downwards, called positive deflection) at the same M_∞ when $\alpha > \alpha_s$, because the downwash flow field near the wing trailing edge is improved by the increasing δ_ϕ. Figure 4b illustrates the comparison of the pressure distribution on the upper surface of the wing on conditions of $\delta_\phi = 0$ and $\delta_\phi = 15$ deg at $M_\infty = 0.8$ and $\alpha = 20$ deg (the distribution of pressure-measuring section and position on the upper surface of wing are shown in Fig. 1a). It can be found from Fig. 4b that the bursted vortex can be improved to some extent owing to the decreased adverse pressure gradient in the flow

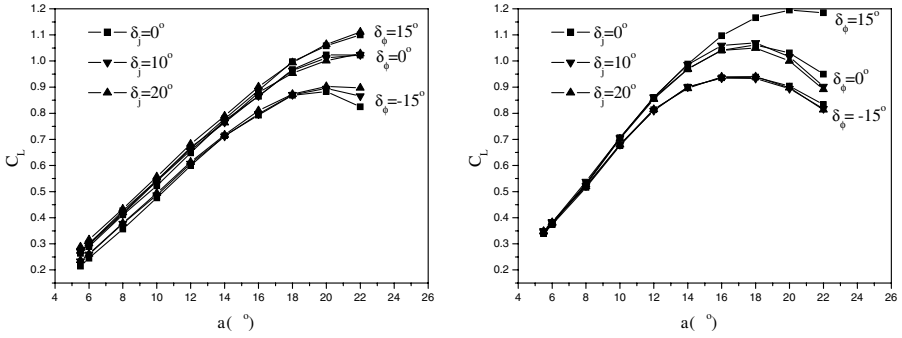

a) $M_\infty = 0.4$ **b) $M_\infty = 0.8$**

Fig. 3 The curve of C_L of the forebody changing with α at jet off.

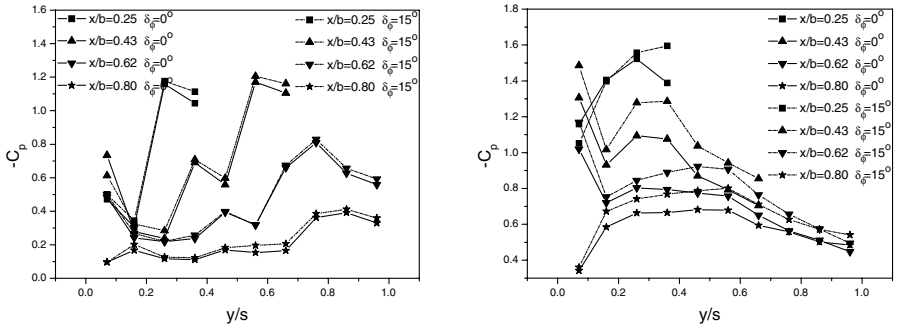

a) $\alpha = 8^o$ **b) $\alpha = 20^o$**

Fig. 4 The curve of C_p changing with y/s on the upper wing surface under different δ_ϕ without jet ($M_\infty = 0.8$).

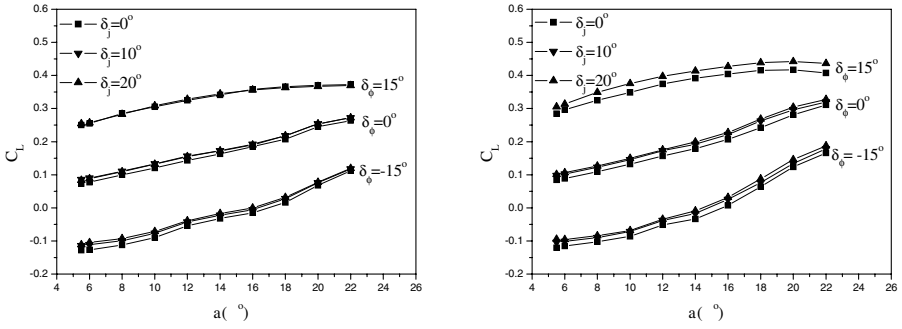

a) $M_\infty = 0.4$ **b) $M_\infty = 0.8$**

Fig. 5 The variation of C_L of the afterbody with α at jet off.

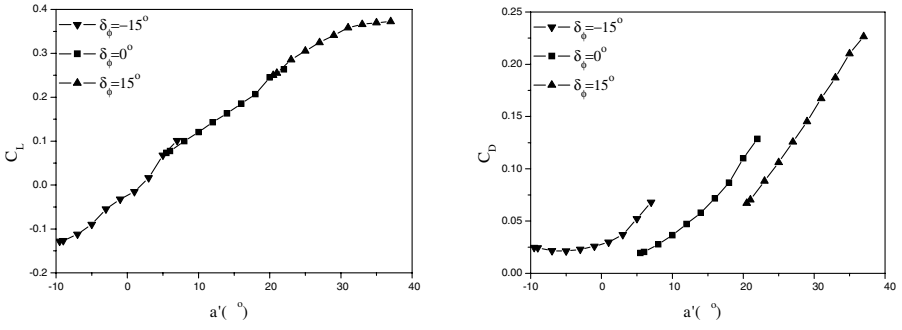

a) The afterbody C_L changing with α' **b) The afterbody C_D changing with α'**

Fig. 6 The curve of force coefficient of the afterbody changing with α' at jet off ($\delta_j = 0$ deg $M_\infty = 0.4$).

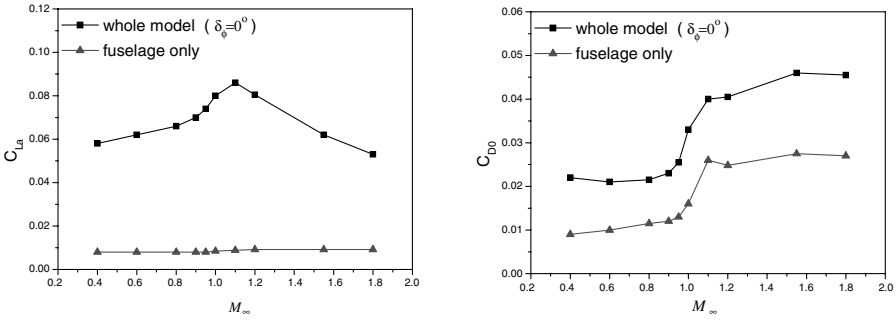

a) $C_{L\alpha}$changing with M_∞ **b) C_{D0} changing with M_∞**

Fig. 7 The force comparison of whole model with the fuselage alone under different Mach number at jet off.

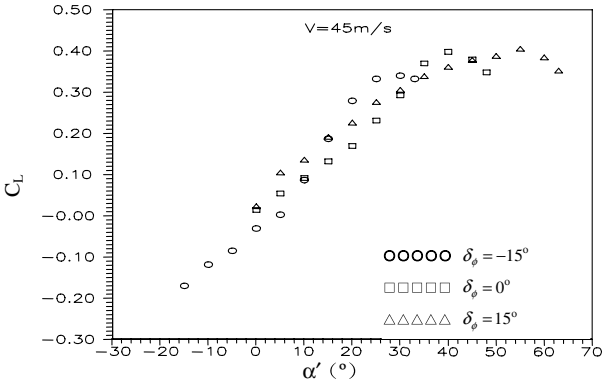

Fig. 8 The curve of C_L of afterbody changing with effect angle of attack α' at jet off ($V_\infty = 45$ m/s).

field near the wing trailing edge by comparing the solid line ($\delta_\phi = 0$ deg) with dot line ($\delta_\phi = 15$ deg), and the decreased adverse pressure gradient is caused mainly by the positive deflection of the horizontal tail. Additionally, attention must be paid that this effect of δ_ϕ on the forebody C_L is limited only when $\alpha > \alpha_s$ by comparing the effect when $\alpha = 8$ deg (shown in Fig. 4a) with that when $\alpha = 20$ deg (shown in Fig. 4b). Figure 4a shows that the effect of δ_ϕ on the stable vortex flow over forebody when $\alpha = 8$ deg is very weak. Moreover, this effect is also stronger when $M_\infty = 0.8$ than that when $M_\infty = 0.4$ at the same α by comparing Fig. 3a with Fig. 3b.

2. Aerodynamic Characteristics of Afterbody Without Jet

The variation of afterbody lift coefficient C_L with angle of attack on conditions of different M_∞ and jet off is shown in Fig. 5. It shows that as following:

1) The afterbody lift coefficient C_L increases with increasing δ_j (when the exit of nozzles is deflected downwards, called positive deflection) because the effective curvature of the afterbody is increased caused by the increasing δ_j. And this effect of δ_j on the afterbody lift is more obviously at $M_\infty = 0.8$ than that at $M_\infty = 0.4$.

2) Lift coefficient C_L of the afterbody increases with the increasing δ_ϕ. Therefore, a concept of effective angle of attack α' is presented for analyzing lift behavior of the afterbody in the following equation:

$$\alpha' = \alpha + \delta_\phi \tag{3}$$

Where α is the angle of attack of the model. The deflection angle of horizontal tail δ_ϕ can be considered to have the same function as α in this present special case, which has been proved in Fig. 6a, because the horizontal tail is the main contributor to the afterbody lift as shown in Fig. 7a, in which the whole model consists of fuselage and horizontal tail. But it should be noted that this concept is not suitable to the drag behavior, as shown in Figs. 6b and 7b, in which the drag of the fuselage is the primary component of the whole model. In addition, the similar conclusion can also be drawn from the low speed test of this model (illustrated in Fig. 8).

3. The Flow Patterns over the Model Without Jet

From the present experimental investigation, there are three different flow patterns over the model from Figs. 3, 6, and 8.

1) *Attached flow*: In the region of $\alpha' < 8$ deg for afterbody and $\alpha < 4$ deg for forebody, the flows are attached on the model surface and the lift coefficient C_L is a linear function of the angle of attack α' or α. Figure 9 shows the pressure isobar of the upper surface of the horizontal tail when $V_\infty = 45$ m/s at jet off. Figure 9a illustrates the attached flow over the horizontal tail at $\alpha' = 0$ deg with obviously adverse pressure gradient.

2) *Vortex-controlled flow*: At the middle angle of attack, 8 deg $< \alpha' <$ 30 deg for afterbody and 4 deg $< \alpha <$ 14 deg for forebody at $M_\infty = 0.8$, the flow over the model separates from the leading edge of wing or horizontal tail and forms the stable vortices around the model. Figure 9b shows the stable vortex-controlled flow over the horizontal tail. The pressure isobar of the upper surface of the wing without jet-on conditions of $M_\infty = 0.8$ and $\delta_\phi = 0$ deg is illustrated in Figs. 10, 10a, and 10b and shows the stable vortex-controlled flow over the wing. Therefore nonlinear vortex lift is induced and the upper limit of the angle of attack in this region increases as the M_∞ decreases, such as 4 deg $< \alpha <$ 18 deg for forebody at $M_\infty = 0.4$.

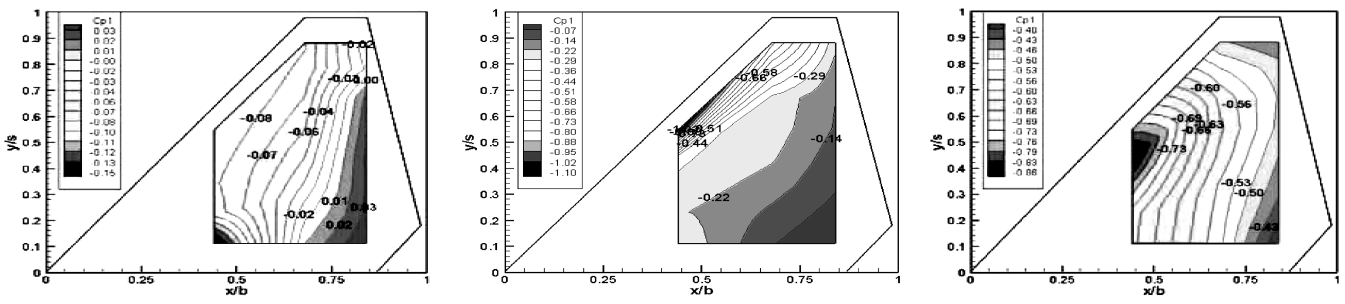

a) $\alpha' = 0°$ **b) $\alpha' = 25°$** **c) $\alpha' = 40°$**

Fig. 9 The pressure isobar of the upper surface of the horizontal tail without jet ($V_\infty = 45$ m/s).

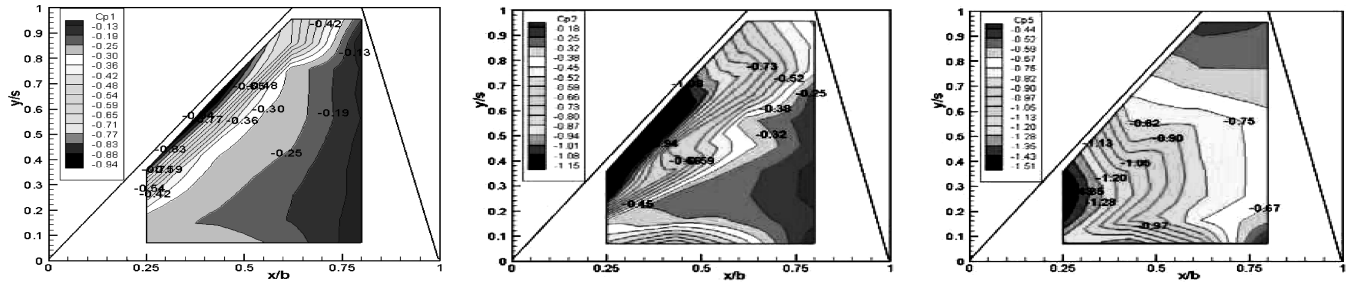

a) $\alpha = 4^{\circ}$ b) $\alpha = 8^{\circ}$ c) $\alpha = 20^{\circ}$

Fig. 10 The pressure isobar of the upper surface of the wing without jet ($M_\infty = 0.8\ \delta_\phi = 0$ deg).

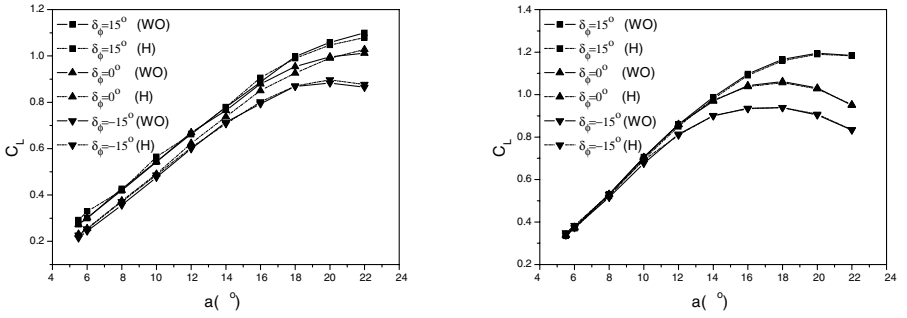

a) $\delta_j = 0^{\circ}$ $M_\infty = 0.4$ b) $\delta_j = 0^{\circ}$ $M_\infty = 0.8$

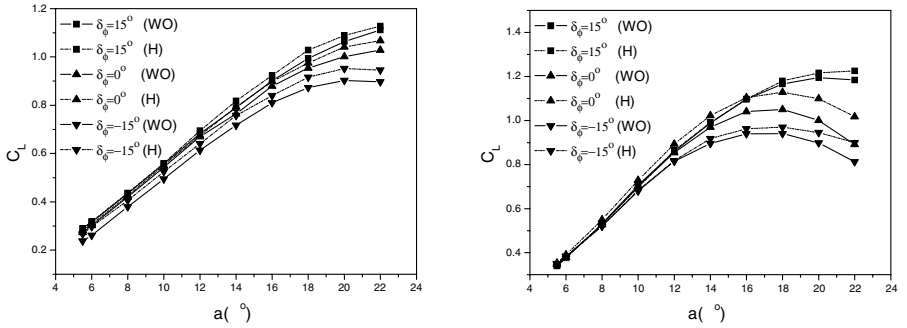

c) $\delta_j = 20^{\circ}$ $M_\infty = 0.4$ d) $\delta_j = 20^{\circ}$ $M_\infty = 0.8$

Fig. 11 The variation of forebody lift C_L with α on conditions of jet on (NPR = 2.1) and jet off (NPR = 1).

3). *Bursted vortex-controlled flow*: At high angle of attack the model has stalled due to the bursted leading edge vortices above the wing and horizontal tail. On these conditions, the slope of lift curve $C_{L\alpha}$ (or $C_{L\alpha'}$) decreased quickly, even $C_{L\alpha} \leq 0$ (or $C_{L\alpha'} \leq 0$). The flows over the forebody on condition of $\alpha > 14$ deg and $M_\infty = 0.8$ belong to this type, and does it over the afterbody at $\alpha' > 30$ deg when $v = 45$ m/s. Moreover, the stalled angle of attack α_s increases with the freestream speed decreasing. Figures 9c and 10c show the bursted-vortex flow over the horizontal tail and wing, respectively.

B. Aerodynamic Characteristics of Model with Vectoring Jet

Because of the different type of mainflow patterns around the model, the vectoring jet effects on the aerodynamic behaviors of model is also distinct. According to this, the effects of vectoring jet on the aerodynamic characteristics of the model can be given as follows:

1. Jet Effect on Attached and Vortex-Controlled Flow

1) *Jet effect on forebody*: Figure 11 shows the comparison of forebody lift C_L changing with angle of attack on conditions of jet on (NPR = 2.1, NPR stands for the nozzle pressure ratio, and NPR = 1 refers to jet off and the same in the following figures) and jet off (NPR = 1) at various parameters δ_j, δ_ϕ, and M_∞, in which the dot line (labeled as H) represents the forebody lift C_L on conditions of $M_\infty \neq 0$ and jet on except for direct thrust component and solid line (labeled as WO) represents the forebody lift C_L on conditions of $M_\infty \neq 0$ and jet off, respectively. Namely, the difference of the forebody lift C_L between these two test conditions (labeled as H and WO) is the jet-induced or supercirculation effect of the vectoring jet on the flow field over the model. By comparing Fig. 11b with Fig. 11d, it is clearly shown that the jet-induced effect on forebody C_L at $M_\infty = 0.8$ is increased with the jet angle δ_j increasing form 0 to 20 deg when $\alpha < 14$ deg, namely in the regions of attached and vortex-controlled flow. And it is the same as on conditions of $\alpha < 18$ deg and $M_\infty = 0.4$ by comparing Fig. 11a with Fig. 11c. But the jet-induced effect of δ_j on forebody lift is small and changes little with the angle of attack α and freestream Mach number on conditions of the attached and vortex-controlled flows. Figure 12 gives the comparison of pressure distribution on upper wing surface between $\delta_j = 0$ deg and $\delta_j = 20$ deg at $\alpha = 12$ deg when $M_\infty = 0.8$ on conditions of jet on (NPR = 2.1) and jet off (NPR = 1). As a result, it is easy to understand the above conclusions by comparing the pressure distribution above the wing surface at jet on (dot line) and jet off (solid line) in the region of vortex-controlled flow field.

2) *Jet effect on afterbody*: Figure 13 presents the variation of jet-induced effect on aerodynamic characteristics of afterbody with respect to jet deflection angle δ_j at $\alpha = 20$ deg, $M_\infty = 0.8$ and

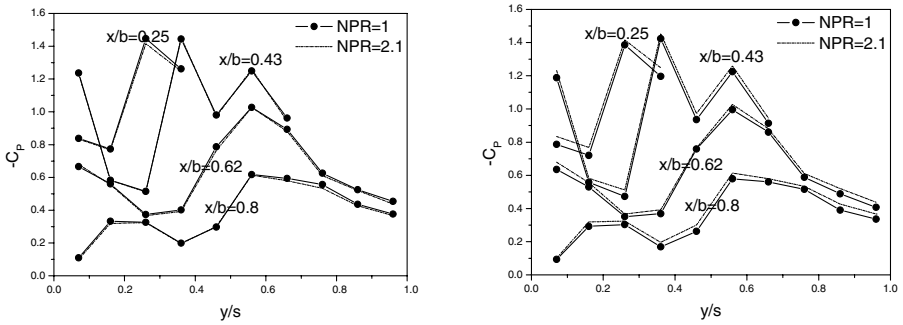

a) $\alpha = 12^\circ\ \delta_j = 0^\circ$ b) $\alpha = 12^\circ\ \delta_j = 20^\circ$

Fig. 12 The pressure distribution on upper wing surface at different δ_j on conditions of jet on (NPR = 2.1) and jet off (NPR = 1) ($M_\infty = 0.8$).

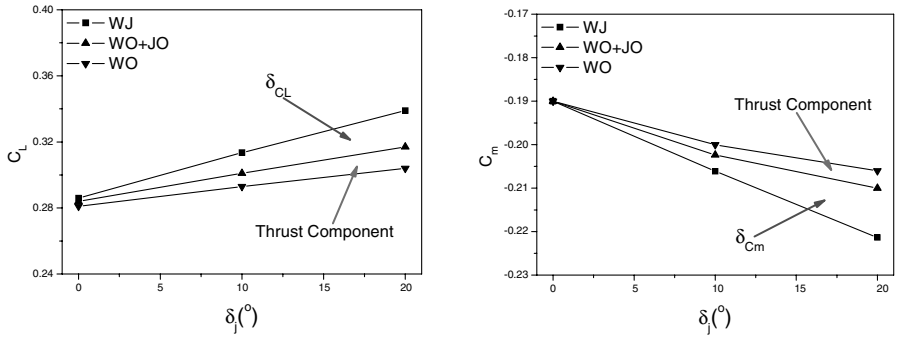

a) The variation of afterbody lift C_L with δ_j b) The variation of afterbody pitching moment C_m with δ_j

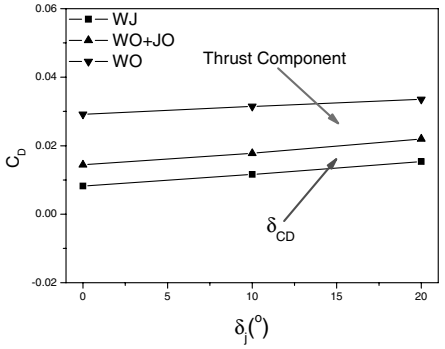

c) The variation of afterbody drag C_D with δ_j

Fig. 13 The jet-induced effect ($\alpha = 20$ deg, $\delta_\phi = 0$ deg, $M_\infty = 0.8$, NPR = 2.1).

$\delta_\phi = 0$ deg, where δ_{CL}, δ_{Cm}, and δ_{CD} are the jet-induced or supercirculation effect of vectoring jet-on afterbody lift, pitching moment and drag, respectively, as shown in Eq. (1). It can be found that the jet-induced effects on the afterbody changes obviously with δ_j, especially for the lift C_L and pitching moment C_m. The jet-induced effect δ_{CL} and δ_{Cm} can even exceed the corresponding value of direct thrust components of the afterbody C_L and C_m, moreover the jet-induced effect values can reach to about 10% of the total C_L and C_m acting on the afterbody at $M_\infty = 0.8$ and $\delta_j = 20$ deg. In addition, the jet-induced effect on the drag of the afterbody is also obvious, as illustrated in Fig. 13c, in which the jet-induced decrement of δ_{CD} nearly accounts for 30% of the total direct thrust component for drag at $M_\infty = 0.8$.

The jet-induced effect δ_{CL} on the afterbody changing with α at different jet deflection angle δ_j and horizontal-tail deflection angle δ_ϕ at $M_\infty = 0.8$ and NPR = 2.1 are shown in Fig. 14. It can be found from it that the jet-induced effect δ_{CL} on the afterbody increases with increasing δ_j nonlinearly and the jet-induced effect δ_{CL} is almost kept constant when $\delta_j > 20$ deg. In addition, it is noted that the angle of attack α almost has no effect on the δ_{CL} in the attached and stable vortex-controlled flows.

Figure 15 shows the comparison of jet effect on the pressure distribution of the upper surface of the horizontal tail between $\delta_j = 0$ and $\delta_j = 20$ deg on conditions of $\delta_\phi = 0$ deg, $\alpha = 20$ deg, and $M_\infty = 0.8$ (the pressure-measuring section and position distribution are shown in Fig. 1b). The jet-induced increment of the negative

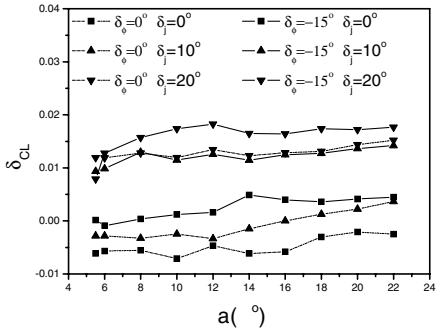

Fig. 14 The variation of jet-induced effect on afterbody with α at different δ_j and δ_ϕ ($M_\infty = 0.8$, NPR = 2.1).

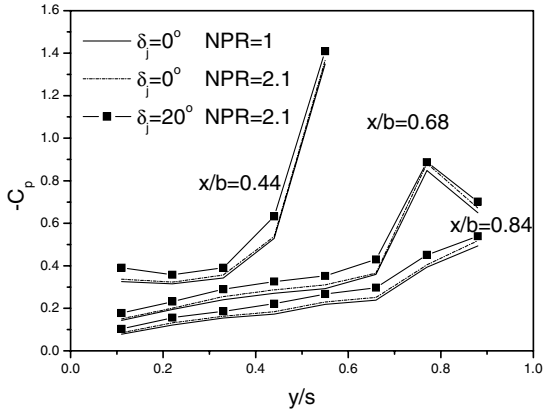

Fig. 15 The jet effect on the pressure distribution of the horizontal tail at different δ_j ($\delta_\phi = 0$ deg $\alpha = 20$ deg $M_\infty = 0.8$).

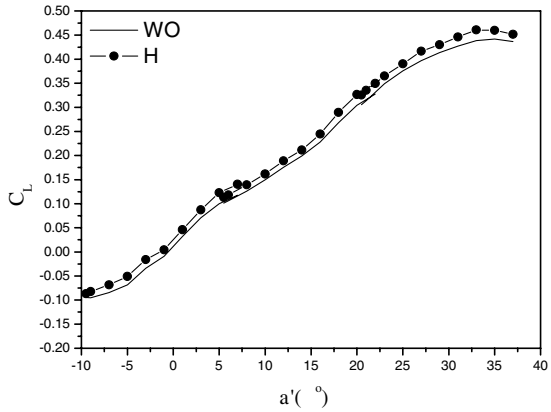

Fig. 17 The variation of afterbody C_L with α' at jet on (NPR = 2.1) and jet off (NPR = 1) ($M_\infty = 0.8$ $\delta_j = 20$ deg).

pressure above the surface increases with δ_j increasing by comparing the dot line (NPR = 2.1) and solid line (NPR = 1), but the jet-induced effect changes little along the span and chord of the horizontal tail.

From the above discussion, an important conclusion can be drawn that the jet-induced effect on the afterbody is more obvious than that on the forebody when the flow over the model is controlled by attached or stable vortex flow. Moreover the jet-induced effect changes little with angle of attack, Mach number and along the span and chord of the wing or horizontal tail.

2. Jet Effect on Bursted Vortex-Controlled Flow

1) *Jet effect on forebody*: It can also be found from Fig. 11 that the jet-induced effect on forebody C_L increases obviously with the jet deflection angle δ_j increasing while the angle of attack $\alpha > \alpha_s$ ($\alpha_s = 18$ deg at $M_\infty = 0.4$ and $\alpha_s = 14$ deg at $M_\infty = 0.8$). Moreover, this jet-induced effect can account for about 10% of the total forces acting on the forebody at $\delta_j = 20$ deg and $\alpha = 22$ deg, as shown in Fig. 11d. It is the reason that the bursted vortices above the wing surface can be improved to some extent by the injection effect of the vectoring jet. It can be found by comparing the pressure distribution on the upper wing surface on conditions of jet on (NPR = 2.1) and jet off (NPR = 1) at $M_\infty = 0.8$, $\alpha = 20$ deg and $\delta_\phi = 0$ deg, as shown in Fig. 16, in which the dot and solid line stands for test results on condition of jet on (NPR = 2.1) and jet off (NPR = 1), respectively. It can be found from Fig. 16 that the bursted vortices over the wing can be improved obviously by the bigger jet deflection, such as $\delta_j = 20$ deg and NPR = 2.1, as shown in Fig. 16b, in which a larger negative pressure peak is obtained, whereas it cannot be found on condition of $\delta_j = 0$ deg, as shown in Fig. 16b.

2) *Jet effect on afterbody*: Figure 17 shows the variation of afterbody C_L with α' on conditions of jet on (NPR = 2.1) and jet off (NPR = 1) at $M_\infty = 0.8$ and $\delta_j = 20$ deg, where the dash-symbol line and solid line refer to jet on (NPR = 2.1) and jet off (NPR = 1) cases, respectively. It can be found from Fig. 17 that the leading edge vortices begin to burst above the horizontal-tail surface when $\alpha' \geq 30$ deg. As a result, the slope of lift curve $C_{L\alpha'}$ decreases and nearly $C_{L\alpha'} \leq 0$ when $\alpha' > 30$ deg, in other words the afterbody of this fighter configuration has stalled when $\alpha' \geq 30$ deg. Therefore the effect of vectoring jet-on afterbody in the bursted-vortex flow region is stronger than that in the attached and vortex-controlled flow region ($\alpha' < 30$ deg) at the same jet deflection angle $\delta_j = 20$ deg and the jet-induced effect increases with the increasing α' as shown in the Fig. 17.

With the α' increasing, the jet-induced effect δ_{CL} becomes very obvious at a high angle of attack in a low speed test as shown in Fig. 18. In the range $\alpha' > 40$ deg, not only the jet-induced effect δ_{CL} increases obviously with α' increasing, but also δ_{CL} changes clearly with the pressure ratio NPR. From the pressure distribution on the upper surface of the horizontal tail as shown in Fig. 19 (in which the dot and solid line stands for pressure distribution with and without jet, respectively), we can find that the vectoring jet can recover the bursted vortex to some extent which induces the larger lift increment at high angle of attack.

Therefore, a conclusion can be made that the vectoring jet can improve the bursted-vortex flows obviously at high angle of attack and the jet-induced effects are not only on the afterbody but also on the forebody.

IV. Conclusions

Thrust vectoring is one of the very important technologies to develop the 4th generation fighter. The present study is to investigate the interactions between the vectoring jet and main flow around the aircraft. The interaction behavior strongly depends on the fighter geometry configuration. Several conclusions can be drawn from the above investigation about the jet-induced effect on the aerodynamic characteristics of this fighter configuration as follows:

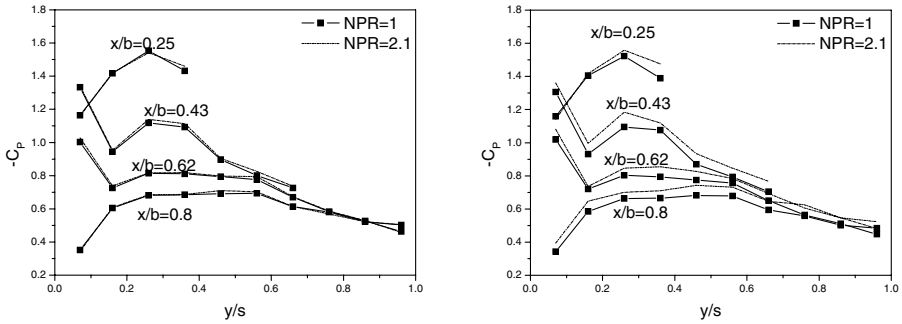

Fig. 16 The pressure distribution on the upper wing surface at different δ_j on conditions of jet on (NPR = 2.1) and jet off (NPR = 1) ($M_\infty = 0.8$, $\delta_\phi = 0$ deg).

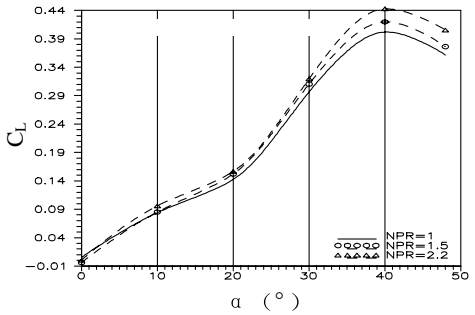

Fig. 18 The variation of afterbody C_L with α' at jet on (NPR = 2.1) and jet off (NPR = 1) ($\delta_j = 20$ deg $V_\infty = 45$ m/s).

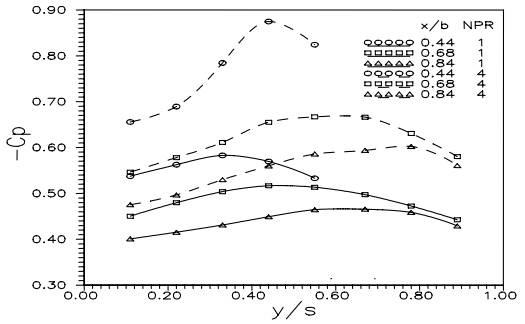

Fig. 19 The jet effect on the bursted vortex above the upper surface of the horizontal tail ($\alpha = 45$ deg $\delta_j = 20$ deg $V_\infty = 45$ m/s).

1) The flow pattern around this fighter configuration can be divided into three types: attached, stable vortex-controlled and bursted-vortex-controlled flows.

2) There are differences among the jet-induced effects on these three flow patterns. First, the jet effect on the fighter configuration increases with increasing δ_j when $\delta_j < 20$ deg and almost keeps constant at $\delta_j > 20$ deg in the attached and stable vortex-controlled flows, and the angle of attack α and freestream Mach number M_∞ have little effect on the interactions between the vectoring jet and main flow in these flow patterns. Second, the jet effects on the aerodynamic characteristics of fighter controlled by the bursted-vortex flow are stronger than that in attached and stable vortex-controlled flows. Moreover, the jet-induced effect changes with δ_j, α, and M_∞ obviously. The bursted vortices will be improved to some extent due to the vectoring jet.

3) The jet-induced effect can even exceed the corresponding values of direct thrust component and accounts for about $10 \sim 30\%$ of the total aerodynamic forces or moments acting on the model at high angle of attack.

4) The deflection angle of vectoring jet δ_j is the main parameter influencing the interaction behaviors between the vectoring jet and main flow around the fighter configuration. The angle of attack α and freestream Mach number M_∞ only determine the flow patterns around the configuration.

5) A concept of effective angle of attack α' is introduced to discuss the lift and pitching moment acting on the afterbody because the forebody and after-fuselage have little effect and contribution to them. But it failed to be applied to the drag because the after-fuselage is the main contributor for the afterbody drag.

References

[1] Kitowski, J. V., "Fighter Airframe/Propulsion Integration: A General Dynamic Perspective," AIAA Paper 92-3332, July 1992.

[2] Mace, J., and Gregory Nyberg, "Fighter Airframe/Propulsion Integration: A McDonnell Aircraft Perspective," AIAA Paper 92-3333, July 1992.

[3] Mishler, R., and Wilkinson, T., "Emerging Airframe/Propulsion Integration Technologies at General Electric," AIAA Paper 92-3335, July 1992.

[4] Liston, G. W., and Small, L. L., "Fighter Airframe/Propulsion Integration: A Wright Laboratory Perspective," AIAA Paper 92-3337, July 1992.

[5] Xueying, D., "The Study of Effects of Vectoring Jet Parameters," Beijing University of Aeronautics & Astronautics, BH-B3942, 1990.

[6] Xueying, D., "The Effects of Vectoring Jet on Aerodynamic Behaviors of Modern Fighter," Beijing University of Aeronautics & Astronautics, BH-B371, 1990, pp. 2–11.

[7] Sheu, W.-L., and Lan, C. E., "Experimental Investigation of the Effect of Thrust Vectoring on Lateral-Directional Aerodynamics at High Angles of Attack," A94-1809, 1994.

[8] Asbury, S. C., and Capone, F. J., "Thrust Vectoring Characteristics of the F-18 High Alpha Research Vehicle at Angles of Attack from 0 to 70," AIAA 92-3095, July 1992.

[9] Coates, P., "Investigation of Thrust Vectoring and Post-Stall Capability in Air Combat," AIAA 88-4160, Aug. 1998.

[10] Capone, F. J., and Berrier, B. L., "Investigation of Axisymmetric and Nonaxisymmetric Nozzles Installed on a 0.10-Scale F-18 Prototype Airplane Model," NASA TP-1638, June, 1980.

[11] Mason, M. L., and Berrier, B. L., "Static Investigation of Several Yaw Vectoring Concepts on Nonaxisymmetric Nozzles," NASA TP-2432, June, 1985.

[12] Capone, F. J., Mason, M. L., and Leavitt, Laurence D., "An Experimental Investigation of Thrust Vectoring Two-Dimensional Convergent–Divergent Nozzles Installed in a Twin-Engine Fighter Model at High Angles of Attack," NASA TM-4155, Feb. 1980.

[13] Capone, F. J., Mason, M. L., and Carson, G. T., Jr., "Aeropropulsive Characteristics of Canted Twin Pitch-Vectoring Nozzles at Mach 0.20 to 1.20," NASA TP-3060, May, 1991.

[14] Mason, M. L., and Berrier, B. L., "Static Performance of an Axisymmetric Nozzle with Post-Exit Vanes for Multiaxis Thrust Vectoring," NASA TP-2800, May 1988.

[15] Mason, M. L., Capone, F. J., and Asbury, S. C., "A Static Investigation of the F/A-18 High Alpha Research Vehicle Thrust Vectoring System," NASA TM-4359, 1992.